The final publication is available at

http://doi.org/10.1007/s11244-018-1030-2

Additional Information

Hydrogenation of CO$_2$ on nickel-iron nanoparticles under sunlight irradiation

Alberto V. Puga*, Avelino Corma*

Instituto de Tecnología Química (Universitat Politècnica de València – Consejo Superior de Investigaciones Científicas), Av. de los Naranjos s/n, 46022 Valencia, Spain

apuga@itq.upv.es, acorma@itq.upv.es
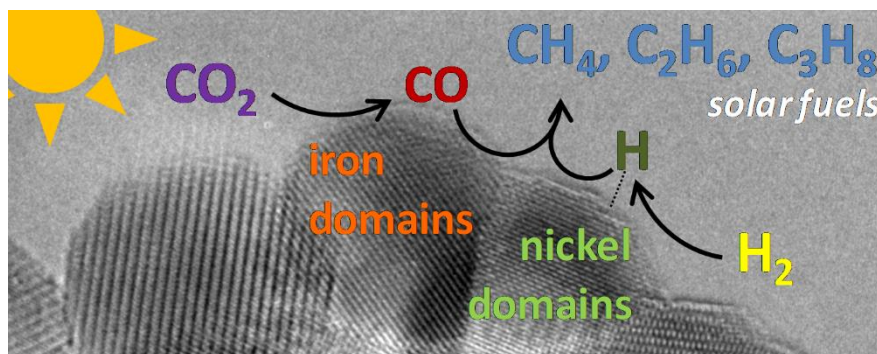
Abstract

Nickel-iron oxide nanoparticles were prepared by a simple mixed oxalate precursor decomposition method and used as catalysts for the sunlight-promoted CO$_2$ hydrogenation reaction. The composition of the Ni$_y$Fe$_{1-y}$O$_x$ materials was designed to cover the entire Ni/Fe ratio range (y = 1, 0.9, 0.75, 0.5, 0.25, 0.1, 0). Characterisation was undertaken by means of elemental analyses, X-ray diffraction (XRD) and high resolution transmission electron microscopy (HRTEM). The pure nickel material (NiO$_x$) contained crystalline NiO nanoparticles. Upon introducing lower proportions of iron in Ni$_9$FeO$_x$ and Ni$_3$FeO$_x$, NiO was the only crystalline phase, along with increasing amounts of amorphous iron oxides. Higher iron contents resulted in the co-existence of NiO and γ-Fe$_2$O$_3$ domains at the nanoscale in NiFeO$_x$, NiFe$_3$O$_x$ and NiFe$_9$O$_x$, whereas the pure iron material (FeO$_x$) was composed of α-Fe$_2$O$_3$ as the only crystalline phase and a significant fraction of amorphous iron oxides. The hydrogenation of carbon dioxide was tested on the materials under simulated sunlight irradiation, and the activities and selectivities investigated as initial CO$_2$ conversion rates and product distributions, respectively. The introduction of iron was beneficial for the activation of CO$_2$, due to the known ability of this metal for promoting the reverse water-gas shift (rWGS) reaction. On the other hand, it was proven that nickel and iron favoured hydrogenation and chain growth processes, respectively. Moreover, the lack of hydrogenation sites in the pure iron material results in the expected preferential generation of olefins. Results for the entire compositional range draw a clear trend towards the enhanced formation of short-chain alkanes at middle iron contents, most likely owing to the existence of junctions of nickel and iron oxides at the nanoscale, and the related interfaces providing rWGS, chain growth and hydrogenation sites in close vicinity. The

resulting hydrocarbon products, presumably produced by the efficient combination of thermal and photonic effects, can be considered as solar fuel replacements to natural gas and liquefied petroleum gases.

1   Introduction

The utilisation of carbon dioxide as a feedstock is called to become a key strategy in the context of sustainability of the chemical industry in the impending scenario of declining fossil carbon resources, chiefly crude oil and natural gas [1-2]. A particular approach which deserves special attention is the transformation of CO_2 into fuels and chemicals via hydrogenation [3-6]. These processes can be regarded as truly sustainable on the condition that hydrogen is obtained using renewable resources and energy, as for example from the dissociation of water powered by photovoltaic or wind-derived electricity [7]. The production of valuable carbon-based substances obtained in this manner may represent an incentive to the capture and recycling of CO_2 from the many gigantic emission sources of this greenhouse gas [1].

As stated above for hydrogen generation, alternatives to the exploitation of fossil resources should rely as much as possible on renewable primary energy sources, and solar radiation appears as one of the most abundant, widespread and versatile options [8-9]. In this context, the exclusive utilisation of solar energy and renewable feedstocks for the production of fuels is a promising strategy [10-11]. These so-called solar fuels can indeed be carbon-based substances derived from CO_2, thus being suitable to directly replace fossil-derived liquid or condensable fuels widely used as energy carriers in transportation or power generation. Regarding the sources of energy needed to power the conversion of CO_2 (*e.g.* via hydrogenation), the use of sunlight ultimately renders a totally renewable process [12-14].

Reduction of carbon dioxide by hydrogen has been shown to take place on different metallic oxide nanoparticles under concentrated solar light [15]. In that report, it was demonstrated that selectivity depended on the type of metal employed: NiO nanoparticles favoured methanation, Fe_2O_3 or Fe_3O_4 led to the formation of CO as main product and to small amounts of ethane, whereas CoO produced a mixture of CO and CH_4. Activities were found to be highly dependent on particle sizes, morphology and irradiation conditions. Later, the efficiency of photothermal CO_2 methanation using H_2 on alumina-supported catalysts based on a range of metals, especially Ru, Rh, Ni, Co and Pd, was demonstrated [16]. Conversely, iron nanoparticles covered by carbon layers were designed for the transformation of CO_2 into CO under similar conditions, also proving that the surface plasmon resonance effect promoted the photo-generation of charges to trigger the reaction [17]. This is consistent with recent results from our laboratories showing that carbon-coated cobalt nanoparticles can promote the hydrogenation of CO_2 into hydrocarbons and oxygenates owing to a combination of thermal and photonic effects, as suggested by photo-action spectra, hole-trapping experiments and comparative reactions carried out at identical temperatures either in the dark or under irradiation [18]. Based on all the aforementioned investigations, it seems clear that nanoparticles of certain transition metals can

catalyse CO_x hydrogenation reactions via photothermal activation, that is, local heating originated by light absorption [19-21]; notwithstanding this, photonic pathways cannot be ruled out for these solar-driven processes entailing materials with strong UV-vis absorption profiles, via either plasmon effects of metallic nanoparticles [17] or bandgap excitation of semiconductor oxides [15]. Other nanostructured materials effecting the sunlight-initiated hydrogenation of carbon dioxide are those based on ruthenium supported on silicon nanowires [22], $In_2O_{3-x}(OH)_y$ nanoparticles [23], or silicon nanocrystals [24]. Regarding reactor engineering, recirculation of gaseous feeds [25] or the design of twin membrane setups [26] represent interesting options.

The benefits of bimetallic materials for the catalytic CO_2 hydrogenation reaction, stemming from the combination of appropriate sites over the different metal surfaces, have been reported on a range of combinations. The addition of nickel to noble metals was shown to facilitate methanation on ceria-or alumina-supported catalysts [27]. This is not surprising considering the suitability of nickel materials for providing highly active hydrogenation sites enhancing the production of methane from CO/H_2 or CO_2/H_2 mixtures [28]. On the other hand, cobalt [29] and iron [30-31] are well-known for promoting chain growth towards the formation of hydrocarbons in Fishcer-Tropsch processes, that is, via CO hydrogenation. The main difference between cobalt and iron catalyst is the proven ability of the latter to activate the reverse water-gas shift (rWGS) reaction [6, 32], that is, the transformation of CO_2 into CO. For this reason, the design of iron materials appears as a valid approach to optimise the activity and selectivity of catalysts for the production of hydrocarbons from CO_2. Examples of cobalt-iron materials have been successfully applied to CO_2 hydrogenation for the production of light olefins, due to the limited hydrogenation ability of iron-rich materials [33-34]. Improvements in C_{2+} selectivities have also been recently achieved on cobalt-iron materials under UV-vis irradiation [20]. Considering the characteristic performances of the aforementioned metals, it can be inferred that combining the high CO_2 conversion activity and the chain growth promotion of iron, and the proven efficiency of nickel for promoting hydrogenation and chain termination reactions, can be viewed as a convenient technology to generate short-chain hydrocarbon products by hydrogenation of carbon dioxide. Although this has been proven for the analogous Fischer-Tropsch reaction [35], the utilisation of nickel-iron catalysts for the transformation of CO_2/H_2 into hydrocarbons remains largely unexplored.

In this work, we aim at systematically studying the activity and selectivity trends over the entire range of Ni/Fe ratios for the sunlight-promoted hydrogenation of carbon dioxide. To this end, bimetallic nickel-iron oxide nanomaterials ($Ni_yFe_{1-y}O_x$) were produced by a simple oxalate decomposition (pyrolysis). The goal is to ascertain whether, in addition to methane, lower alkanes can be also efficiently obtained using inexpensive materials and solar irradiation as the only energy input to the process. This is expected to represent a pathway toward the production

of solar fuels which might serve as replacements to natural gas (generally a mixture of methane and ethane) and liquefied petroleum gases (chiefly C_{3-4} alkanes), relying on renewable feedstocks and energy.

2   Experimental

2.1.   Materials

Nickel(II) acetate tetrahydrate ($\geq$ 99.0%), iron(II) acetate (95%), oxalic acid (98%) were supplied by Sigma-Aldrich, and used as received. Ethanol absolute (reagent grade) was supplied by Scharlau and used as received. The gases used for the reactions under simulated sunlight irradiation, H_2, CO_2 ($\geq$ 99.995%), and N_2 were supplied by Linde (HiQ grade).

2.2.   Synthesis of nickel-iron nanoparticles

The designed nickel-iron oxide nanoparticles were prepared by the thermal decomposition of oxalate intermediates, previously obtained by a sol-gel method. In a typical synthesis, appropriate amounts of nickel(II) acetate tetrahydrate and iron(II) acetate (Ni/Fe molar ratios spanning from 0 to 1, according to the data in Table 1) were dissolved in ethanol under constant stirring for 1 h at 45 °C, yielding solutions exhibiting colours ranging from reddish to bright green upon increasing nickel content. An oxalic acid solution (200 mL, 0.23 M) in ethanol was then added slowly to the warm sol to yield brown-greenish to turquoise gels. After evaporating the solvent at 80–110 °C overnight, the corresponding oxalates were obtained as bright green solids. Subsequent calcination under static air atmospheres at 500 °C (2 °C min^{-1}) for 3 h yielded the final $Ni_yFe_{1-y}O_x$ nanoparticulated materials, which are hereinafter coded as shown in Table 1.

Table 1. Summary of the synthesis of $Ni_yFe_{1-y}O_x$ materials.[a]

	$\chi(Ni)/\chi(Fe)$	$wt(Ni(OAc)_2 \cdot 4H_2O)/g$	$wt(Fe(OAc)_2)/g$
NiO_x	1.00:0.00	0.9995	-
Ni_9FeO_x	0.90:0.10	0.8933	0.0694
Ni_3FeO_x	0.75:0.25	0.7369	0.1717
$NiFeO_x$	0.50:0.50	0.4831	0.3376
$NiFe_3O_x$	0.25:0.75	0.2376	0.4982
$NiFe_9O_x$	0.10:0.90	0.0941	0.5920
FeO_x	0.00:1.00	-	0.6535

[a] The materials were prepared according to the nominal metallic ratio expressed as $\chi(Ni)/\chi(Fe)$ and following the synthetic procedure described in the text starting from the specified amounts of nickel and/or iron precursors.

2.3. Characterisation

X-ray diffraction (XRD) measurements were performed by means of a PANalytical Cubix'Pro diffractometer equipped with an X'Celerator detector and automatic divergence and reception slits using Cu-Kα radiation (0.154056 nm). The mean size of the ordered (crystalline) domains (ϕ) was estimated using the Scherrer equation. The equation can be written as $\phi = \frac{0.9\,\lambda}{\beta\,cos\theta}$ where λ is the X-ray wavelength, β is the line broadening at half the maximum intensity (FWHM), after subtracting the instrumental line broadening, in radians, and θ is the Bragg angle. Characterization by high-resolution transmission electron microscopy (HRTEM) was carried out in a JEM-2100 LaB$_6$ (JEOL) microscope, at an accelerating voltage of 200 kV, coupled with an Inca Energy TEM 200 (Oxford) energy dispersive X-ray (EDX) spectroscopy and a high-angle annular dark field (HAADF) detector. Samples were deposited on carbon-coated copper grids. Average sizes and standard deviations were calculated by determining diameters for a minimum of forty particles in HRTEM images by using the Image J software. Metal contents were determined by inductively coupled plasma (ICP) analyses performed on a Varian 715-ES ICP Optical Emission Spectrometer. Diffuse reflectance UV–vis (DRUV–vis) absorption spectra were carried out on a CARY 500 SCAN VARIAN spectrophotometer in the 300–800 nm range.

2.4. Sunlight-promoted CO$_2$ hydrogenation

Photoassisted CO$_2$ hydrogenation under simulated sunlight irradiation in the presence of the catalyst solid powders (75 mg) were carried out in purpose-designed quartz cells (V = 50 cm^3). After evacuating the cell (P < 10 mbar), appropriate amounts of CO$_2$, N$_2$ and H$_2$ (typically, 20, 20 and 100 cm^3, standard conditions; the initial total pressure typically reached *ca.* 2.7 bar) were introduced. Simulated sunlight irradiations of the solids were carried out using a solar simulator (Newport®, Oriel Instruments, model 69921) equipped with a Xe lamp (1000 W) coupled with an AM1.5 filter that provides concentrated simulated sunlight. Unless otherwise noted, the irradiance at the surface of the solids was *ca.* 50 kW m^{-2}. Under these conditions, temperatures at the surface of the solids increased up to a maximum of *ca.* 300 °C, in a similar fashion to experiments reported for other similar light-driven systems [16-17, 19-20]. The time-profile conversion of the reactions was followed by analysing samples (2 cm^3) taken from the gas phase periodically on a two-channel chromatograph (Agilent 490 Micro GC, carrier gas: Ar) equipped with thermal conductivity detectors (TCD), and a MS 5Å column (first channel) for the quantification of H$_2$, N$_2$ and CO, and a PoraPLOT Q column (second channel) for the quantification of CO$_2$ and C_{2-3} hydrocarbons. The analyses were verified and complemented for C_{4+} products using a three-channel chromatograph (Varian 450-GC Rapid Refinery Gas Analyser) equipped with one TCD for the quantification of H$_2$ (first channel), one TCD for the

quantification of CO_2 and CO (second channel), and one flame ionisation detector (FID) for the quantification of hydrocarbons (third channel); the carrier gases were Ar (first channel) and He (second and third channels)

3   Results and Discussion

3.1.   Composition of the Ni$_y$Fe$_{1-y}$O$_x$ nanoparticles

As described in the Experimental section, nickel-iron nanoparticles were prepared by thermal decomposition (T = 500 °C) of oxalate precursors at appropriate metallic ratios. The solids were obtained as powders exhibiting colours from dark grey for NiO$_x$, to brown-red for increasing iron contents, and finally to red-orange for FeO$_x$ (see Figure 1, top). The formation of crystalline phases was investigated by XRD, as shown in Figure 1 (bottom).
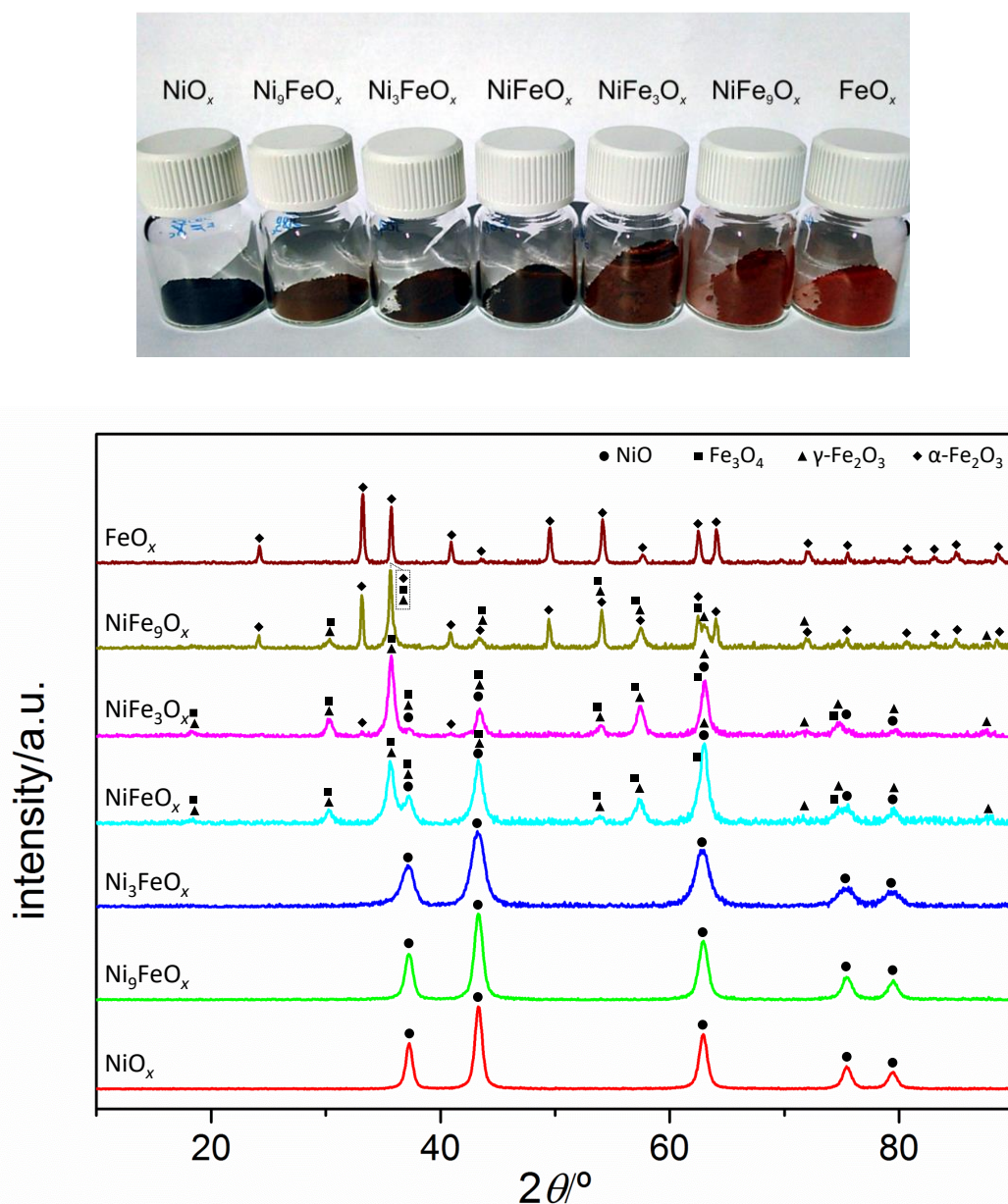

Figure 1. Photographs showing the aspect (top), and X-ray diffractograms (λ = 0.154056 nm, bottom) of the Ni$_y$Fe$_{1-y}$O$_x$ materials. Diffraction peaks were identified and assigned to the phases indicated according to the X'Pert High Score Plus software.

For the pure nickel material, calcination leads to the formation of cubic NiO nanoparticles. By increasing iron contents up to a 25% Fe metallic ratio (Ni_9FeO_x and Ni_3FeO_x), no other phases could be observed, and the samples became somewhat less crystalline, as suggested by decreasing signal-to-noise ratios. Thus, iron species were presumably residing in amorphous domains or in extra-small crystallites. Furthermore, the sizes of NiO nanoparticles decreased, as further commented below. The equimolar $NiFeO_x$ material still contained a significant proportion of NiO, in addition to iron oxides, among which cubic maghemite (γ-Fe_2O_3) was prevalent. Signal overlapping prevented concluding about the formation of small amounts of magnetite (Fe_3O_4), and this possibility cannot be ruled out, as suggested by the identification of its characteristic diffractions (see for example the shoulder at 62.7 ° in Figure 1). The syntheses of materials containing higher amounts of iron resulted in the formation of hematite (α-Fe_2O_3). In $NiFe_3O_x$, a mixture of the three mentioned iron oxides, with traces of NiO_x, was formed, whereas $NiFe_9O_x$ contained predominantly hematite and smaller amounts of maghemite and possibly magnetite; no crystalline nickel species could be identified. Finally, hematite was the only crystalline phase observed in FeO_x. Throughout the entire series of iron-containing materials, significant amounts of amorphous iron oxides might be also present, as suggested by elemental analyses and HRTEM (see below). It should be noted that there was no sign of crystallised mixed nickel-iron oxides, based on these XRD data.

Absorption profiles obtained by DRUV-vis spectroscopy (Figure S1, Supplementary Material) show the expected absorption edges for iron-containing materials at *ca*. 550 nm (corresponding to the known bandgap of Fe_2O_3 close to 2.2 eV [36]), whereas the counterparts containing NiO crystallites presented edges at around 350 nm (corresponding to the characteristic bandgap for this compound at ca. 3.5 eV [36]). Furthermore, the pure nickel material absorbed light throughout the entire visible range, probably indicating the presence of metallic nickel nanoparticles. It should be pointed out that, although the CO_2 hydrogenation activities are likely to be significantly ascribed to photothermal effects, the strong light absorption capabilities of the $Ni_yFe_{1-y}O_x$ materials studied herein might also be partly responsible for the observed performance, as proven for carbon-coated cobalt [18] or iron [17] nanoparticles.

In addition to the presence of crystalline phases described above, the elemental composition of the materials determined by ICP revealed that variable amounts of amorphous sub-stoichiometric oxides may be present, given that the oxygen contents ($x \leq 0.90$ in $Ni_yFe_{1-y}O_x$, see Table S1) are all below the expected values for mixtures of NiO, Fe_2O_3 and/or Fe_3O_4 ($x = 1.00$–1.50, theoretical range). This reinforces the probability, as mentioned above, of existence of amorphous oxides, most likely in partially reduced states, and thus implies the formation of oxygen vacancies in the materials to a significant extent.

3.2. Morphology and particle sizes of the $Ni_yFe_{1-y}O_x$ nanoparticles

The thermal decomposition of the precursor oxalates gave rise to the formation of the corresponding nickel or iron oxide nanoparticles with sizes below 50 nm in all cases, as evidenced by particle size determinations performed from XRD measurements (see Table 2). The results were reasonably coincident with those obtained from multiple measurements performed by HRTEM (data shown in Table 2 and images in Figure 2 and Figures S2–S8). Deviations might be due in part to the fraction of amorphous domains, especially for samples with higher amount of iron, which were less crystalline.

Table 2. Particle sizes of $Ni_yFe_{1-y}O_x$ nanoparticles.

		ϕ/nm	
	phase	XRD[a]	HRTEM[b]
NiO_x	NiO	11.2	12.5 ± 4.4
Ni_9FeO_x	NiO	9.7	12.1 ± 3.9
Ni_3FeO_x	NiO	6.4	7.7 ± 2.5
$NiFeO_x$	NiO	8.4[c]	6.0 ± 1.5
	γ-Fe_2O_3	12.6	13.9 ± 4.6
$NiFe_3O_x$	γ-Fe_2O_3	13.4	14.5 ± 5.4
	α-Fe_2O_3	25.9	-
$NiFe_9O_x$	γ-Fe_2O_3	11.9	14.2 ± 4.1
	α-Fe_2O_3	33.1	-
FeO_x	α-Fe_2O_3	29.6	39.8 ± 13.7

[a] Average diameters of crystalline domains was estimated using the Scherrer equation as described in Section 2.3, ($\phi = 0.9\lambda/\beta\cos\theta$; λ: X-ray wavelength, β: broadening at half the maximum intensity, and θ: Bragg angle), using the diffractions at 43.3, 35.7 and 33.2 ° for NiO, γ-Fe_2O_3 and α-Fe_2O_3, respectively. [b] Average diameters and standard deviations determined from the measurement of a minimum of thirty particles. [c] Due to overlapping with a γ-Fe_2O_3 diffraction signal, the error for the calculated NiO diameter might be large.

The NiO particle sizes in the pure nickel material (NiO_x) were within the 8–17 nm range, and decreased upon increasing iron content to 5–10 nm for Ni_3FeO_x (see Table 2). A detailed view of a region showing the co-existence of crystalline, partly coalesced, NiO nanoparticles of irregular

shape in close vicinity to amorphous domains is illustrated in Figure 2 (top left) for Ni$_9$FeO$_x$. More images showing this kind of morphology are shown in Figures S2–S4). The material consisting on a 1:1 Ni/Fe metallic mixture (NiFeO$_x$) contains, according to XRD results, NiO and γ-Fe$_2$O$_3$ nanocrystals of diameters around 8.4 and 12.6 °, respectively. Observations made by HRTEM allowed the identification of NiO nanocrystals ranging 4–8 nm, and distinguishably larger γ-Fe$_2$O$_3$ particles ranging 9–19 nm. The difference in NiO particle sizes calculated from either XRD or HRTEM data might stem from the overlap between nickel and iron oxides diffractions for the peak considered (≈ 43 °). In NiFeO$_x$ (Figure S5), and even more noticeably in NiFe$_3$O$_x$ (Figure 2, top right), the presence of intimately contacted NiO and γ-Fe$_2$O$_3$ nanoparticles has been observed by HRTEM. This particular morphology leads to the existence of interfaces between the nickel and iron domains on the surface of the catalyst. As stressed in the Introduction, the former would provide surfaces hosting highly active hydrogenation sites, whereas the latter would exhibit surfaces with actives sites for both the activation of CO$_2$ via rWGS and C-C coupling reactions resulting in the growth of hydrocarbon chains. The catalytic results under simulated sunlight presented below (Section 3.3) confirm the importance of the close co-existence of nickel and iron phases for efficient formation of light paraffins.
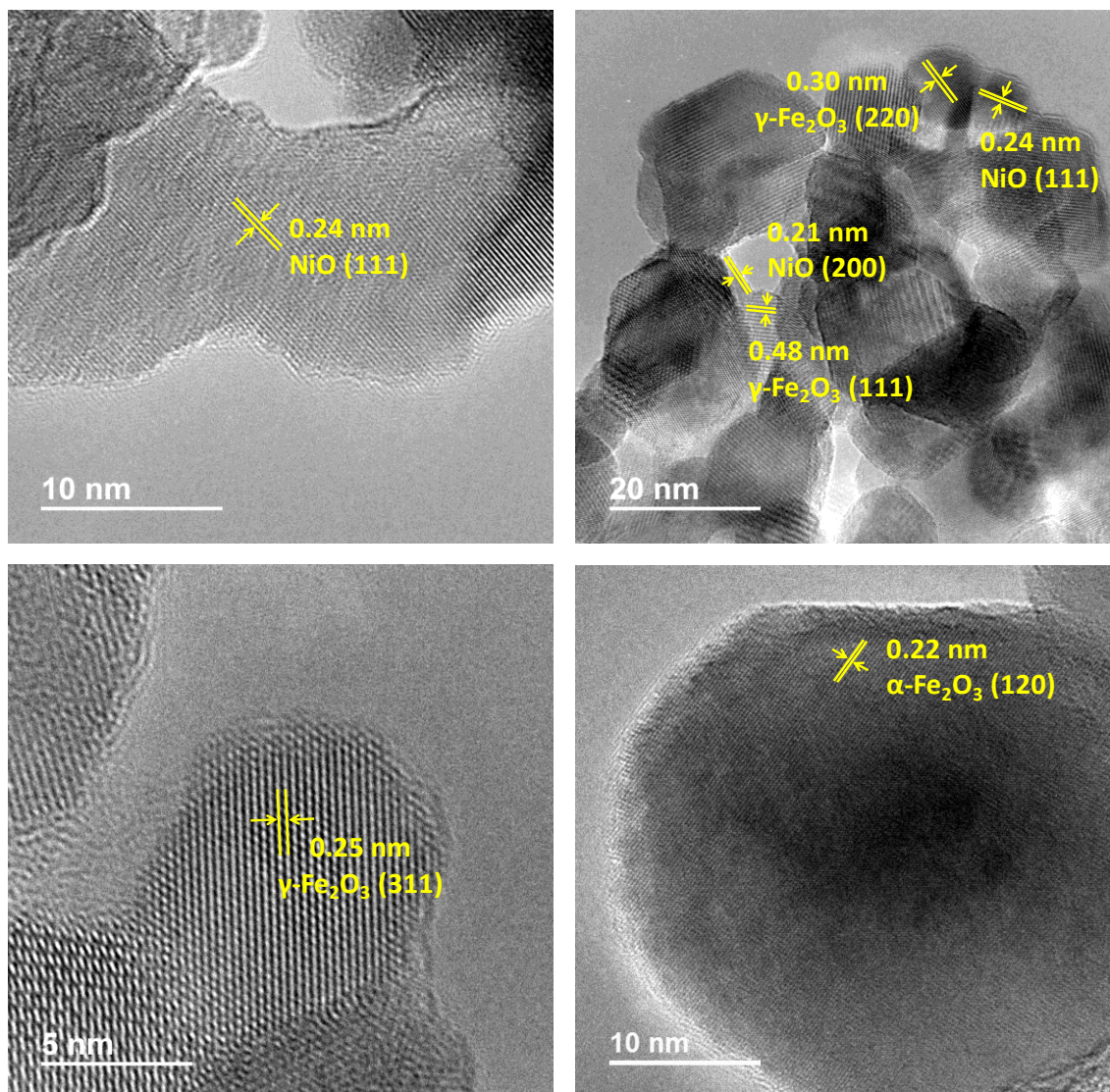
Figure 2. HRTEM micrographs (200 kV) of $Ni_yFe_{1-y}O_x$ materials: Ni_9FeO_x (top left), $NiFe_3O_x$ (top right), $NiFe_9O_x$ (bottom left), and FeO_x (bottom right). Lattice spacing values for the identified crystalline phases are shown on the corresponding images.

The mixed metal material containing a higher proportion of iron ($NiFe_9O_x$) is formed by crystalline γ-Fe_2O_3 and α-Fe_2O_3 nanoparticles of sizes around 11.9 and 33.1 nm, respectively, according to XRD data (see Table 1). The presence of γ-Fe_2O_3 nanoparticles was clearly apparent in HRTEM images, as shown in Figure 2 (bottom left), whereas amorphous material of undefined shape was also noticeable in some areas (see Figure S7). Finally, the pure iron material (FeO_x) was composed mostly of ill-defined, slightly oval, and partly coalesced amorphous iron oxide phases, as shown in Figure S8, in addition to pseudo-spherical crystallised α-Fe_2O_3 particles of relatively large size (> 25 nm, see Figure 2, bottom right).

3.3. Sunlight-Promoted CO₂ Hydrogenation

Results for the hydrogenation of CO_2 under simulated sunlight are summarised in Table 3 for the entire series of $Ni_yFe_{1-y}O_x$ materials. A complete set of raw data for all reactions can be also accessed in the Supplementary Material. The pure nickel nanoparticles (NiO_x) performed as a moderately active methanation catalyst, as expected for nickel materials of this kind [14-15, 28, 37]. Conversion was low (6.7%) after one hour of irradiation, and only methane and a small proportion of carbon monoxide were detected as products. The introduction of 10% metallic iron in Ni_9FeO_x resulted in a noticeably higher activity, as evidenced by a six-fold increase in conversion (up to 40.4%, see Table 3) under identical conditions. A further proof of this is the increase observed in the initial CO_2 conversion rate, as shown in Figure 3. The following counterpart of the nickel-iron nanoparticle series, Ni_3FeO_x, confirmed the trends observed, since the conversion and initial rate increased significantly with respect to Ni_9FeO_x. By increasing iron content, activity was further boosted, as illustrated by the nearly quantitative conversions (> 94%) observed for the materials consisting on Ni/Fe ratios ≤ 1 ($NiFeO_x$, $NiFe_3O_x$ and $NiFe_9O_x$, see Table 3). These results support the rationale exposed in the Introduction about the role of iron species in promoting the conversion of CO_2 into CO, owing to their proven suitability as catalysts for the water-gas shift—and its reverse, rWGS—reaction [5-6, 30]. The presence of increasing amounts of iron favour the activation of CO_2 via the rWGS reaction, thus resulting in initial rates as high as ≈ 6.3 mmol h^{-1} for $NiFe_3O_x$ (Figure 3). Upon further iron enrichment, CO_2 conversions slow down to some extent. It is likely that this decline in activity is due to the scarcity of nickel sites able to dissociate hydrogen, a necessary step previous to removal of adsorbed oxygen via hydrogenation and subsequent desorption of water, which is the rWGS reaction by-product. However, efficiencies are maintained to some extent, even for the pure iron material, which exhibits an initial CO_2 conversion rate around 2.5 mmol h^{-1} (see Figure 3).

Table 3. Catalytic performance of the $Ni_yFe_{1-y}O_x$ nanoparticles in sunlight-promoted CO_2 hydrogenation reactions.[a]

catalyst	conversion(CO_2)/%	selectivity/%				olefin/paraffin ratio
		CH_4	C_{2-3}	C_{4+}	CO	
NiO_x	6.7	90.8	-	-	9.2	-
Ni_9FeO_x	40.4	87.3	0.6	-	12.1	-
Ni_3FeO_x	73.6	95.0	2.2	-	2.8	-
$NiFeO_x$	94.1	77.7	19.6	2.0	0.7	< 0.01
$NiFe_3O_x$	95.8	79.8	17.5	1.1	1.6	< 0.01
$NiFe_9O_x$	94.5	75.3	20.8	1.0	2.8	< 0.01
FeO_x	70.8	35.0	25.6	2.3	37.1	2.9

[a] Reaction conditions: catalyst amount: 75 mg; cell volume: 50 cm^3; gaseous feed mixture: $CO_2/N_2/H_2$ (20:20:100 cm^3, standard conditions); irradiation: simulated sunlight (Xe lamp, 1000 W, AM1.5 filter, *ca.* 50 kW m^{-2}); reaction time: 1 h.
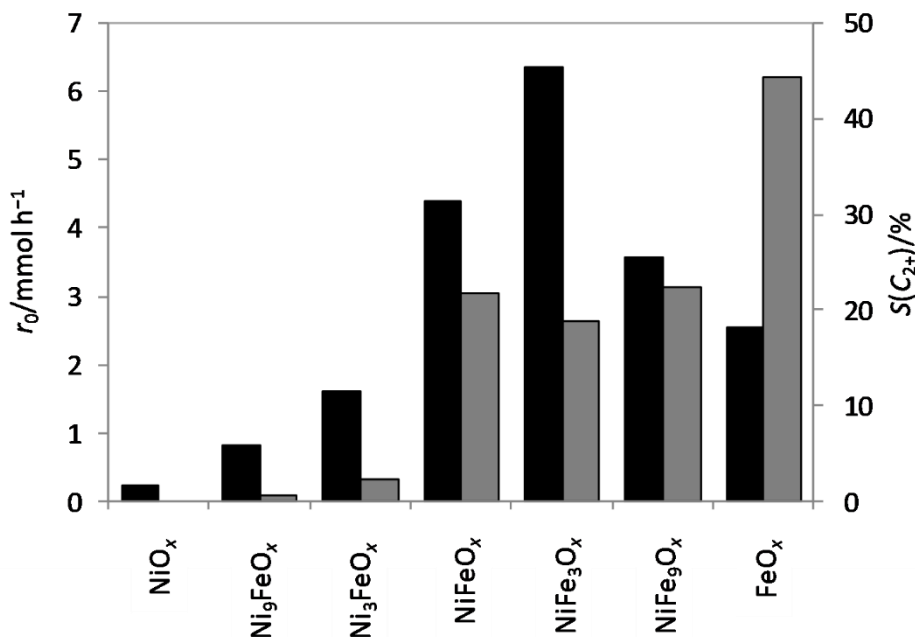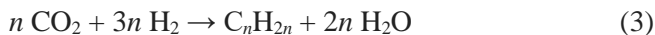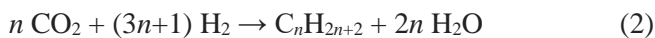

Figure 3. Initial CO_2 conversion rate (r_0, black bars) and hydrocarbon selectivity towards C_{2+} products ($S(C_{2+})$, excluding CO, grey bars) obtained from CO_2 hydrogenation experiments on the series of $Ni_yFe_{1-y}O_x$ materials. Experimental conditions as in Table 3.

At this point, we checked whether the sunlight-promoted CO_2 hydrogenations observed proceeded according to the expected stoichiometries, as listed in the following equations:

$$CO_2 + 4\,H_2 \rightarrow CH_4 + 2\,H_2O \qquad (1)$$
$$n\,CO_2 + (3n+1)\,H_2 \rightarrow C_nH_{2n+2} + 2n\,H_2O \qquad (2)$$
$$n\,CO_2 + 3n\,H_2 \rightarrow C_nH_{2n} + 2n\,H_2O \qquad (3)$$

The oxidation half reactions in these processes involve the oxidation of H_2 into water. This fact was apparent since significant amounts of condensed water were observed on the walls of the cells during and after the irradiations. Given that quantification of water was cumbersome for our system, we proved the stoichiometries by determining the consumed H_2/CO_2 ratios, which were close to four on all instances, consistent with the theoretical range (see equations 1–3). For example, for $NiFe_3O_x$, H_2 conversion was 73.9%, corresponding to a consumed H_2/CO_2 ratio of ~3.9.

Regarding the mode of activation, the reactions can be triggered by a combination of photothermal and purely photonic effects derived from the absorption of sunlight by the nickel-iron nanoparticles, as mentioned in both the Introduction and Section 3.1. In this work, rather than studying the discernment of these primary activation mechanisms (which will be the topic of further investigations), we turned our attention to the influence of the metallic composition on activity and selectivity, especially on the elucidation of which active sites are favoured depending on the Ni/Fe ratio. These issues are discussed in detail in the following paragraphs.

As mentioned above, nickel promotes methanation, and thus, no other hydrocarbons are detected during irradiation of NiO_x. Incorporation of iron leads to the production of light hydrocarbons, thus proving that iron species are able to promote chain growth processes. For example, traces of ethane were produced in addition to methane as the major product and CO as by-product when using Ni_9FeO_x. The amount of $C_{2–3}$ products (ethane and a smaller amount of propane, see Supplementary Material for a complete set of product data) increased to 2.2% for Ni_3FeO_x. However, the ubiquity of nickel domains in these materials, preferentially crystalline NiO based on XRD and HRTEM observations (see Sections 3.1 and 3.2 above), provide abundant hydrogenation sites resulting in high methane selectivities (95.0% for Ni_3FeO_x, see Table 3). The selectivity to C_{2+} products was greatly improved for the materials of the series containing both NiO and γ-Fe_2O_3 phases in close vicinity (see Section 3.2 above), that is, $NiFeO_x$ and $NiFe_3O_x$. Based on these results, it appears that, in addition to being the most active due to the combination of hydrogenation and rWGS sites (see above), these materials contained iron domains clearly suited for the oligomerisation of discrete carbon adsorbates to form short-chain hydrocarbons, chiefly alkanes. The selectivities to hydrocarbons are further increased for

higher iron contents, at the expense of lower activities. In particular, the pure iron counterpart (FeO_x) produced a large amount of CO, as expected taking into account its presumably high rWGS activity and the lack of hydrogenation sites due to the absence of nickel. Notwithstanding this, the hydrocarbon (CO-free) selectivity to C_{2+} products using FeO_x was highest among the series (*ca.* 44%).

The different kinetic behaviour of the catalysts clearly results in discerning them into three main groups, as can be observed in the conversion-selectivity plots shown in Figure 4 (see Supplementary Material for a complete set of data). Those whereby crystalline NiO dominates (NiO_x, Ni_9FeO_x and Ni_3FeO_x) produce CO as a primary product which rapidly hydrogenate to completion to methane with negligible chain growth. Materials with co-existence of nickel and iron oxides at the nanoscale ($NiFeO_x$, $NiFe_3O_x$ and $NiFe_9O_x$) promote rapid CO_2 conversion and both methanation and oligomerisation reactions. The pure iron oxide material (FeO_x) leads to the production of CO via the rWGS reaction, and short-chain products (with predominance of olefins, olefin/paraffin ration: 2.9, Table 3) at moderate to high conversions (see Figure 4).
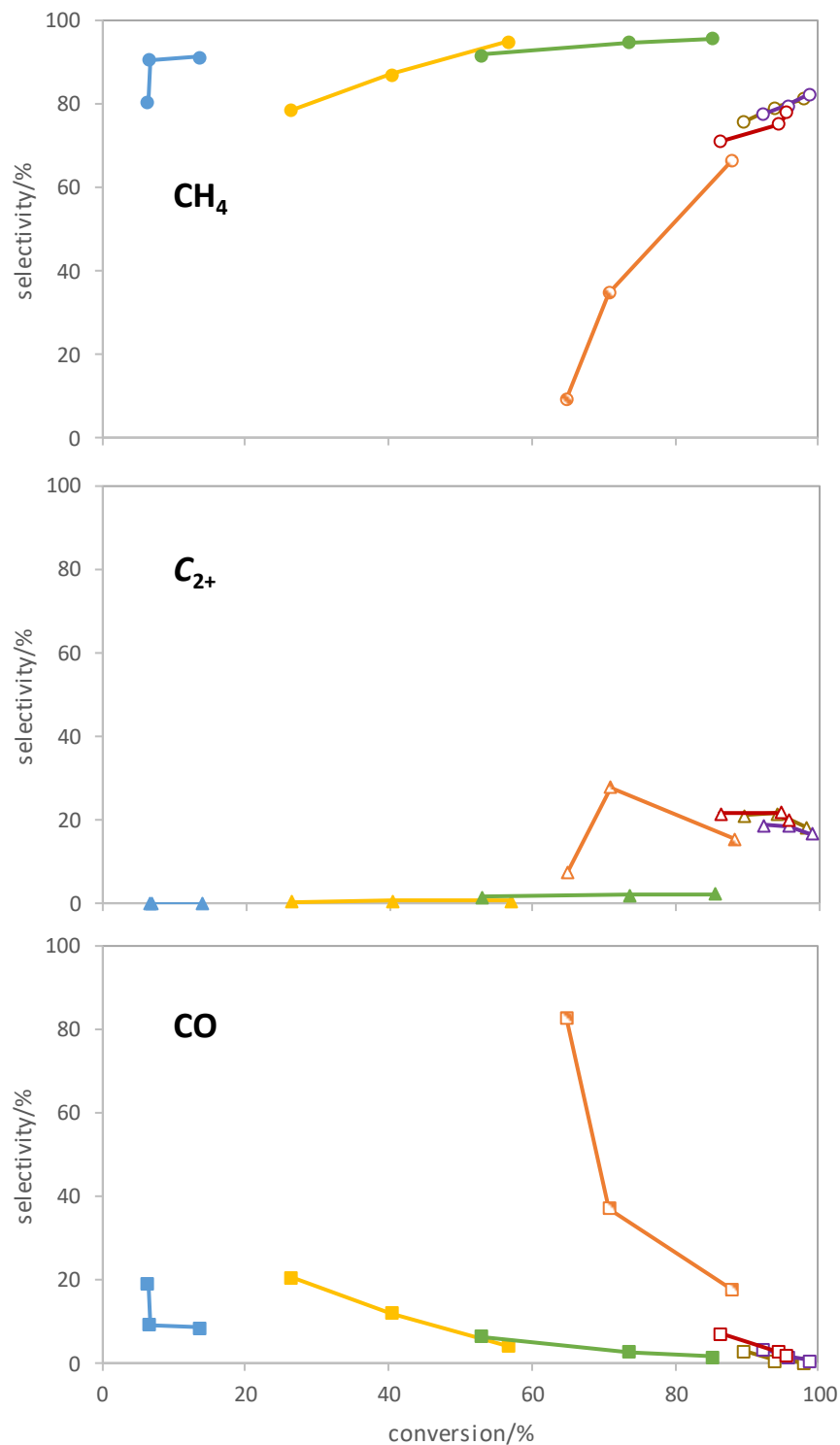
Figure 4. Conversion-selectivity plots for the sunlight-promoted CO_2 hydrogenation products on $Ni_yFe_{1-y}O_x$ materials. blue: NiO_x; yellow: Ni_9FeO_x; green: Ni_3FeO_x; brown: $NiFeO_x$; purple: $NiFe_3O_x$; red: $NiFe_9O_x$; orange: FeO_x. The materials have been categorised into three distinct groups according to their kinetic behaviour: moderately active methanation (NiO_x, Ni_9FeO_x and Ni_3FeO_x; filled symbols), highly active hydrocarbon production ($NiFeO_x$, $NiFe_3O_x$ and $NiFe_9O_x$; empty symbols), and enhanced CO/olefin production (FeO_x; striped symbols).

In view of designing an efficient sunlight-promoted process for the production of light alkanes comprising significant amounts of short-chain paraffin products, the use of mixed nickel-iron catalyst appears as a suitable strategy based on the results presented above. Carbon dioxide conversions can be enhanced by nanoscale combination of carefully adjusted proportions of iron and nickel components, promoting CO_2 deoxygenation (rWGS reaction) and hydrogenation steps, respectively. The intimate contact between Ni and Fe domains, as for example NiO and γ-Fe_2O_3 nanocrystals (as shown in HRTEM images, Figure 2), or even junctions of crystalline NiO with amorphous iron oxides, might give rise to interfaces whereby the different active sites lie at sufficient proximity to catalyse the different reaction steps in an efficient cascade fashion. Furthermore, the presence of iron also provides active surfaces for chain growth, whereas the high hydrogenation performance of nickel is expected to favour chain termination steps and thus limit oligomerisation to the shorter range of hydrocarbons. This is also the reason why olefin selectivity is negligible for Ni-containing materials, whereas it is boosted to olefin/paraffin ratios above unity for FeO_x (see Table 3).

4   Conclusions

Nickel-iron oxide nanoparticulate materials ($Ni_yFe_{1-y}O_x$) prepared by a facile oxalate pyrolysis method perform efficiently in promoting the CO_2 hydrogenation reaction under simulated sunlight irradiation. By scanning through the full nickel/iron molar ratio, three main groups of catalysts can be distinguished according to their kinetic behaviour, giving rise to different product distributions. The performances of each catalyst group can be related to the phases contained and to distinct nanoscale morphologies. Pure nickel or low nickel materials (NiO_x, Ni_9FeO_x and Ni_3FeO_x) are composed of NiO as the only crystalline phase and promote methanation at moderate rates. By increasing iron content, the materials become more active due to the suitability of the nascent iron oxide phases in facilitating the reverse water-gas shift (rWGS) reaction. The intimate contact between crystalline NiO and γ-Fe_2O_3 (and probably also amorphous iron oxide) domains at the nanoscale in $NiFeO_x$, $NiFe_3O_x$ and $NiFe_9O_x$, proved highly efficient for the generation of light alkanes, which can be used as synthetic fuels in the context of CO_2 consideration as a carbon feedstock, and utilisation of renewable H_2. This is due to the combination oligomerisation and hydrogenation sites, attributed to iron and nickel surfaces, respectively. The absence of nickel in FeO_x resulted in the expected increment in olefin production and higher C_{2+} hydrocarbon selectivity owing to the limited hydrogenation and termination activities on iron.

Acknowledgments

References

1.   Aresta M, Dibenedetto A, Angelini A (2014) Catalysis for the Valorization of Exhaust Carbon: from CO_2 to Chemicals, Materials, and Fuels. Technological Use of CO_2. Chem Rev 114:1709-1742

2.   Centi G, Perathoner S (2009) Opportunities and prospects in the chemical recycling of carbon dioxide to fuels. Catal Today 148:191-205

3.   Porosoff MD, Yan B, Chen JG (2016) Catalytic reduction of CO_2 by H_2 for synthesis of CO, methanol and hydrocarbons: challenges and opportunities. Energy Environ Sci 9:62-73

4.   Dorner RW, Hardy DR, Williams FW, Willauer HD (2010) Heterogeneous catalytic CO_2 conversion to value-added hydrocarbons. Energy Environ Sci 3:884-890

5.   Prieto G (2017) Carbon Dioxide Hydrogenation into Higher Hydrocarbons and Oxygenates: Thermodynamic and Kinetic Bounds and Progress with Heterogeneous and Homogeneous Catalysis. ChemSusChem 10:1056-1070

6.   Wang W, Wang S, Ma X, Gong J (2011) Recent advances in catalytic hydrogenation of carbon dioxide. Chem Soc Rev 40:3703-3727

7.   Centi G, Quadrelli EA, Perathoner S (2013) Catalysis for CO_2 conversion: a key technology for rapid introduction of renewable energy in the value chain of chemical industries. Energy Environ Sci 6:1711-1731

8.   Balzani V, Credi A, Venturi M (2008) Photochemical conversion of solar energy. ChemSusChem 1:26-58

9.   Balzani V, Armaroli N, Energy for a Sustainable World: From the Oil Age to a Sun-Powered Future, Wiley, 2010.

10.   Centi G, Perathoner S (2010) Towards Solar Fuels from Water and CO_2. ChemSusChem 3:195-208

11.   Cook TR, Dogutan DK, Reece SY, Surendranath Y, Teets TS, Nocera DG (2010) Solar Energy Supply and Storage for the Legacy and Nonlegacy Worlds. Chem Rev 110:6474-6502

12.   Izumi Y (2013) Recent advances in the photocatalytic conversion of carbon dioxide to fuels with water and/or hydrogen using solar energy and beyond. Coord Chem Rev 257:171-186

13.   Corma A, Garcia H (2013) Photocatalytic reduction of CO_2 for fuel production: Possibilities and challenges. J Catal 308:168-175

14. Puga AV (2016) Light-Promoted Hydrogenation of Carbon Dioxide—An Overview. Top Catal 59:1268-1278

15. Sastre F, Puga AV, Liu L, Corma A, García H (2014) Complete Photocatalytic Reduction of CO_2 to Methane by H_2 under Solar Light Irradiation. J Am Chem Soc 136:6798-6801

16. Meng X, Wang T, Liu L, Ouyang S, Li P, Hu H, Kako T, Iwai H, Tanaka A, Ye J (2014) Photothermal Conversion of CO_2 into CH_4 with H_2 over Group VIII Nanocatalysts: An Alternative Approach for Solar Fuel Production. Angew Chem-Int Ed 53:11478-11482

17. Zhang H, Wang T, Wang J, Liu H, Dao TD, Li M, Liu G, Meng X, Chang K, Shi L, Nagao T, Ye J (2016) Surface-Plasmon-Enhanced Photodriven CO_2 Reduction Catalyzed by Metal-Organic-Framework-Derived Iron Nanoparticles Encapsulated by Ultrathin Carbon Layers. Adv Mater 28:3703-3710

18. Liu L, Puga AV, Cored J, Concepción P, Pérez-Dieste V, García H, Corma A (2018) Sunlight-assisted hydrogenation of CO_2 into ethanol and C2+ hydrocarbons by sodium-promoted Co@C nanocomposites. Appl Catal, B 235:186-196

19. Li Z, Liu J, Zhao Y, Waterhouse GIN, Chen G, Shi R, Zhang X, Liu X, Wei Y, Wen X-D, Wu L-Z, Tung C-H, Zhang T (2018) Co-Based Catalysts Derived from Layered-Double-Hydroxide Nanosheets for the Photothermal Production of Light Olefins. Adv Mater 10.1002/adma.201800527

20. Chen G, Gao R, Zhao Y, Li Z, Waterhouse GIN, Shi R, Zhao J, Zhang M, Shang L, Sheng G, Zhang X, Wen X, Wu L-Z, Tung C-H, Zhang T (2017) Alumina-Supported CoFe Alloy Catalysts Derived from Layered-Double-Hydroxide Nanosheets for Efficient Photothermal CO2 Hydrogenation to Hydrocarbons. Adv Mater 30:1704663

21. Zhao Y, Zhao B, Liu J, Chen G, Gao R, Yao S, Li M, Zhang Q, Gu L, Xie J, Wen X, Wu L-Z, Tung C-H, Ma D, Zhang T (2016) Oxide-Modified Nickel Photocatalysts for the Production of Hydrocarbons in Visible Light. Angew Chem 128:4287-4291

22. O'Brien PG, Sandhel A, Wood TE, Jelle AA, Hoch LB, Perovic DD, Mims CA, Ozin GA (2014) Photomethanation of Gaseous CO_2 over Ru/Silicon Nanowire Catalysts with Visible and Near-Infrared Photons. Adv Sci 1:1400001

23. Hoch LB, Wood TE, O'Brien PG, Liao K, Reyes LM, Mims CA, Ozin GA (2014) The Rational Design of a Single-Component Photocatalyst for Gas-Phase CO_2 Reduction Using Both UV and Visible Light. Adv Sci 1:1400013

24. Sun W, Qian C, He L, Ghuman KK, Wong APY, Jia J, Jelle AA, O/'Brien PG, Reyes LM, Wood TE, Helmy AS, Mims CA, Singh CV, Ozin GA (2016) Heterogeneous reduction of carbon dioxide by hydride-terminated silicon nanocrystals. Nat Commun 7:

25.   Lo C-C, Hung C-H, Yuan C-S, Wu J-F (2007) Photoreduction of carbon dioxide with H_2 and H_2O over TiO_2 and ZrO_2 in a circulated photocatalytic reactor. Sol Energy Mater Sol Cells 91:1765-1774

26.   Cheng Y-H, Nguyen V-H, Chan H-Y, Wu JCS, Wang W-H (2015) Photo-enhanced hydrogenation of CO_2 to mimic photosynthesis by CO co-feed in a novel twin reactor. Appl Energy 147:318-324

27.   Porosoff MD, Chen JG (2013) Trends in the catalytic reduction of CO_2 by hydrogen over supported monometallic and bimetallic catalysts. J Catal 301:30-37

28.   Gao J, Liu Q, Gu F, Liu B, Zhong Z, Su F (2015) Recent advances in methanation catalysts for the production of synthetic natural gas. RSC Adv 5:22759-22776

29.   Khodakov AY, Chu W, Fongarland P (2007) Advances in the Development of Novel Cobalt Fischer−Tropsch Catalysts for Synthesis of Long-Chain Hydrocarbons and Clean Fuels. Chem Rev 107:1692-1744

30.   Abelló S, Montané D (2011) Exploring Iron-based Multifunctional Catalysts for Fischer-Tropsch Synthesis: A Review. ChemSusChem 4:1538-1556

31.   de Smit E, Weckhuysen BM (2008) The renaissance of iron-based Fischer-Tropsch synthesis: on the multifaceted catalyst deactivation behaviour. Chem Soc Rev 37:2758-2781

32.   Riedel T, Claeys M, Schulz H, Schaub G, Nam SS, Jun KW, Choi MJ, Kishan G, Lee KW (1999) Comparative study of Fischer-Tropsch synthesis with H_2/CO and H_2/CO_2 syngas using Fe- and Co-based catalysts. Appl Catal A 186:201-213

33.   Gnanamani MK, Jacobs G, Hamdeh HH, Shafer WD, Liu F, Hopps SD, Thomas GA, Davis BH (2016) Hydrogenation of Carbon Dioxide over Co-Fe Bimetallic Catalysts. ACS Catal 6:913-927

34.   Satthawong R, Koizumi N, Song C, Prasassarakich P (2015) Light olefin synthesis from CO_2 hydrogenation over K-promoted Fe-Co bimetallic catalysts. Catal Today 251:34-40

35.   Li T, Wang H, Yang Y, Xiang H, Li Y (2014) Study on an iron-nickel bimetallic Fischer-Tropsch synthesis catalyst. Fuel Process Technol 118:117-124

36.   Xu Y, Schoonen MAA (2000) The absolute energy positions of conduction and valence bands of selected semiconducting minerals. Am Mineral 85:543-556

37.   Wang W, Gong J (2011) Methanation of carbon dioxide: An overview. Front. Chem. Sci. Eng. 5:2-10